Embedded 3D Printing of Isotropically Enhanced Lattice Structure with Programmable Elasticity *via* Three-Dimensional Fiber Alignment

Qiyi Chen[1], Siamak S. Shishvan[3], Shuo Zhang[1], Angkur J.D. Shaikeea[3], Ju Young Park[1], Zhenpeng Xu[1], Seokpum Kim[4], Nadim S. Hmeidat[4], Hannelore Hemminger[2], Vikram S. Deshpande[3], Xiaoyu (Rayne) Zheng[1,2]*

[1]Department of Material Science and Engineering, University of California, Berkeley, CA 94720, USA
[2]Department of Civil and Environmental Engineering, University of California, Los Angeles, CA 90095, USA
[3]Department of Engineering, University of Cambridge, Cambridge CB2 1PZ, United Kingdom
[4]Manufacturing Science Division, Oak Ridge National Laboratory, Oak Ridge, TN 37831, USA

* Xiaoyu (Rayne) Zheng

Email: rayne23@berkeley.edu

Keywords: Embedded 3D printing, Fiber alignment, 3D alignment, Performance enhancement, Programmable anisotropy

Abstract:
Engineered composites with fiber orientation in a complete three-dimensional (3D) context are highly desired for maximizing structural performance as they mimic the well-organized fiber arrangement in natural composites. However, most fabrication techniques lack the capability for through-plane (z-axis) alignment, limiting the possibility for structural design and performance optimization. In this study, we present an embedded 3D printing approach that enables complete 3D fiber alignment, including region-specific alignment control along the through-plane direction. Our method utilizes the extrusion and suspension of composite inks within a supporting matrix. By regionally adjusting the ink extrusion rate and nozzle translation rate, we locally manipulated the fiber arrangement within the composite 3D architecture. We demonstrate that the 3D alignment of carbon fibers in a structural composite significantly enhances both mechanical properties and thermal conductivity in the in-plane and through-plane directions. Furthermore, by strategically arranging regional fiber orientations within micro-architected materials, we fabricated metamaterial engineered composites with programmable anisotropy ratio and directional moduli.

Teaser
Embedding 3D aligned fiber in Herschel-Bulkley gel enables metamaterial with new design space in thermal-mechanical properties.

MAIN TEXT

1. Introduction

Anisotropic structures, including fibers, platelets, and rods, are a defining characteristic of composite materials. (*1–5*). Natural composites, such as nacre and bamboo, show that 3D oriented reinforcing fibers not only provide exceptional properties such as high stiffness in all directions, but also tailor the material's mechanical behavior at specific regions for diverse natural environments (*6, 7*). The oriented fibers/platelets can also create shorter pathways for electron mobility to achieve much better thermal and electrical conductivity, which is highly desired for electronics, batteries, packaging applications etc. (*8–10*) Researchers have developed engineered composites that possess the oriented fibers and architectured matrices, such as stacked woven carbon fiber fabrics of reinforced polymer (CFRP) composites exhibiting excellent mechanical strength and lightweight properties (*11, 12*), and short carbon fiber reinforced matrices with significantly enhanced thermal conductivity for fast heat dissipation (*13, 14*). Recent advances in additive manufacturing (AM) have unlocked new possibilities for engineered composites, offering unprecedented design freedoms through the creation of complex three-dimensional architectures (*15–18*). Through the deliberate design of 3D micro-architectures enabled by 3D printing, composites exhibit metamaterial-like behaviors, such as high-strength and stiffness at a fraction of their solid counterparts, impact resistance, negative Poisson ratio, as well as self-sensing and shape morphing.

Despite advances, fiber arrangement within the matrix often remains stochastic, limiting the tunability and optimization of composite properties. Recent efforts have been made to incorporate meso-scale control of particulate orientations in 3D printed matrices to address the challenge. In the extrusion-based printing process, a shear field generated during resin extrusion induces fiber alignment along the printing path, enabling the coupling of fiber arrangement with the printed 3D geometry by tuning the extrusion rate and printing speed (*19, 20*). For example, researchers have developed techniques that control the velocity ratio, defined as extrusion rate over nozzle moving speed, to tune the carbon fiber alignment (*21*). Other fillers, such as cellulose fiber, graphene, boron nitride and others, have also been oriented in designed directions and regions within various thermoplastic and thermoset matrices by fused deposition modeling (FDM) and direct ink writing (DIW) (*22–30*). Due to the layer-by-layer deposition process intrinsic to extrusion based printing, fibers are typically aligned in the x-y plane, while through-plane (z-axis) alignment remains a challenge but is crucial for achieving fully optimized three-dimensional properties. External fields, such as an acoustic field and a magnetic field, have been applied to the liquid resin vat in digital light processing (DLP) to achieve through-plane fiber orientation (*31–33*). These methods, however, are restricted to fibers that respond to external fields(*34*). More critically, the fields were applied uniformly to the entire vat, resulting in a single, uniform fiber orientation throughout the material, regardless of location. This uniformity limits the ability to tune the fiber alignment differently at specific locations in both in-plane and through-plane directions, thereby significantly restricting the design space for creating complex 3D fiber architectures. One significant drawback is the anisotropic nature of the resulting properties, where the strengthening in certain directions comes at the expense of weakened properties in others. By contrast, the excellent properties of natural composites originate from the well-arranged fiber alignment in any 3D directions at any 3D locations. Researchers have also developed curved-slicing coupled with multi-DOF robotic arms to offer through-plane extrusion capability (*35, 36*). However, this method is limited to thermoplastics, as the extruded material needs to be rigid enough to support overhang structures, and only small angles of Z-direction alignment can be achieved due to the gravitational force

exceeding the material's strength. Other methods to achieve the through-plane fiber orientation include applying rotational nozzles which control the fiber alignment in the through-plane rotational direction by tuning the rotation speed (*37*). However, the achieved alignment is still limited to the pre-determined rotational directions, lacking full z-directional freedom.

Here, we present an embedded 3D (EMB3D) printing method that achieves comprehensive particle alignment control simultaneously in both the through-plane and in-plane directions. Unlike prior approaches limited to regional or fixed through-plane fiber orientations, our technique achieves full 3D control, allowing fiber alignment in any direction at various points of ink deposition, which leads to significant property improvement in a complete three-dimensional context. By individually planning extrusion paths in any 3D directions, this method facilitates precise fiber alignment in arbitrary 3D orientations, with independent control at specific locations both within and beyond the x-y plane. Such a level of 3D alignment control surpasses the previously reported methods. Moreover, the synergistic control of fiber alignment and macroscopic architecture design allows the creation of engineered metamaterial composites with highly programmable properties. While carbon fiber (CF) serves as the reinforcing component in our method, our approach can be extended to numerous other anisotropic structures orientations, offering versatile functional properties across diverse areas.

2. Materials and methods

2.1 Composite ink and supporting matrix

The ink is composed of a base resin (bisphenol A diglycidyl ether, DGEBA, Sigma Aldrich), a reactive diluent (neopentyl glycol diglycidyl ether, DGENG, Sigma Aldrich), a curing agent (2-ethyl-4-methylimidazole, Sigma Aldrich), a rheology modifier (fumed silica, CAB-O-SIL TS720, Cabot), and a reinforcing filler carbon fiber (CF, milled carbon fiber, PC 100, E&L Enterprise, Inc, 7 μm in diameter, 120 μm mean length). The mass ratio of DGEBA : DGENG is 1 : 1, and the loading of curing agent, TS 720, CF in regard to the total mass of DGEBA and DGENG is 10 wt%, 8 wt%, and 40 wt%, respectively. To prepare the ink, the mixing was done in a planetary mixer (Thinky mixer) at 2000 rpm. DGEBA, DGENG, and curing agent were first mixed together for 1 min, followed by addition of CF. To ensure a good dispersion, the CF was added with an increment of 10 wt%, each increment was mixed for 1 min. TS720 was then added and mixed for 2 min. The supporting matrix is composed of silicone oil and 5 wt% of rheology modifier (fumed silica, CAB-O-SIL M5, Cabot), prepared by mixing in a planetary mixer at 2000 rpm for 2 min.

2.2 Embedded 3D printing

The as-prepared ink was first loaded into a 15 ml syringe, which was then mounted to the Hyrel 3D printer. All samples were printed using a 620 μm stainless-steel nozzle. The as-prepared supporting matrix was loaded into containers with various sizes for different printing structures. The matrix-filled container was placed on the print stage. The printing paths were manually designed and generated with Gcode. After printing, the matrices with the embedded inks were heated to 80 ºC overnight for complete epoxy curing, followed by the removal and cleaning of the supporting matrix. To adjust the fiber alignment while maintaining the same beam diameter, multiple thinner beams with larger rate ratios, offering better fiber alignment, were extruded together to merge into a single thicker beam that corresponds to a smaller Rr, yielding worsened

fiber alignment. The rate ratio is calculated as Ve/Vt. The Vt is determined by recording the time during which the nozzle travels a fixed distance. Ve is measured by recording the time during which a fixed volume of ink is extruded. This volume extrusion rate is then converted into a linear extrusion rate by dividing the nozzle cross-sectional area. Ve remains consistent during each plunger movement, we used the same syringe, nozzle size, and prepared inks and matrices with the same formulation.

The gcode for the embedded 3D printing was prepared by a custom algorithm that generates toolpaths based on the lattice structure geometry with careful control of extrusion parameters within standard G-code commands. First, we extract all vertices and struts from the lattice structure. Before the nozzle moves to a new position, we implement extruder reversal (G1 E-1.5) to create negative pressure at the nozzle tip. This prevents material from dripping during non-printing movements. After positioning the nozzle at the start point of a strut, we prime the extruder (G1 E1.5) to ensure consistent material flow when printing begins. The actual printing move (G1 command) includes calculated extrusion amount based on the distance and the selected rate ratio, which directly controls the fiber alignment. Additionally, we compute the proper 5-axis coordinates at both the starting and ending points based on each strut's direction vector. At intersection nodes, we added pause commands (G4) with durations determined from our experimental data (Figure S3) to ensure proper bonding between struts.

2.3 Heat transfer measurement

For each sample, the lattice cubes with identical dimensions and the same beam diameter were printed for comparison. The printed lattice cubes were placed onto an Aluminum block, which was heated to a constant temperature of 100 ºC. The top and bottom of the lattices were coated with a thin layer of the corresponding ink to ensure a good contact with the heat source. The temperature of the lattice top and heating time were recorded by using a IR camera (Hti-Xintai high resolution).

2.4 Mechanical property test

Simple cube lattices (10x10x10 cm) were printed for compression test, and rectangular slabs (3x12x120 mm) were printed for flexural test. For the simple cubic compression test, the true modulus of the cubic lattice is adopted, which is computed by dividing the compression force over the total area of the cross-section of four vertical beams. SC/BCC lattices with a size of 3x3x3 unit cells were printed at <001> and <110> orientations for compression tests to obtain the experimental data for anisotropic ratio calculation. Details are shown in Figure S7. The Poisson's ratio is calculated under relative density $\bar{\rho}$ = 0.1 by $v = -\frac{\varepsilon_x}{\varepsilon_z}$, Where ε_x is the strain in X axis and ε_z is the strain in Z axis during compression in the <001> direction. For <001> orientation compression test, lattice in Fig. S6B was printed. For <110> orientation compression test, lattice structure in Fig. S6D was printed. Both lattices are extracted from the SC/BCC lattice structure (Fig. S6A, C). The shear modulus is calculated by using the following equations:

$$G = \frac{1}{\frac{1}{E_{110}} - \frac{1-v}{2E}}$$

Where ν is the Poisson's ratio during the compression at <001> orientation, E is the Young's modulus of <001> orientation and E_{110} is the Young's modulus of <110> orientation. All tests were conducted using Instron 5944 universal testing machine (Instron Corporation, Norwood, MA). The applied loads were measured using the Instron load cell with a load capacity of 2000 N, while displacements were tracked using the integrated encoder connected to the crosshead movement.

2.5 Fiber alignment characterization

The fiber alignment within the carbon fiber–epoxy composites is measured by SEM (FEI Quanta 3D FEG FIB) and X-ray computed tomography (XRCT). Tomographic images were acquired using the XCT microscope Zeiss Versa 510 system, set to an optical magnification of 4x, achieving a spatial resolution of ~1 micron. The tomographs were then segmented in the VGStudioMax 2024.1 software using the paint and segment tool. This segmentation process separates the short carbon fibers from the matrix. To ensure the accuracy of the segmentation, we measured the statistics of fiber thickness and adjusted the segmentation parameters to improve the gray value ranges representing the fibers, distinguishing them from the background matrix. This iterative process continued until the fibers were appropriately segmented. Following segmentation, an erosion operation of one voxel was applied to marginally disconnect intersecting fibers, preventing interference with the subsequent analysis of fiber orientation. A reference orientation was defined along the axial direction aligned with the build direction of the composites (see Fig. S2B). The orientations of the fibers were then calculated using the Fiber Composite Material Analysis module. The results for the 3D orientation distribution relative to the axial direction are shown in Fig. 3 and S2, alongside heat maps of the histogram normalized over the total number of short fibers captured in the analysis.

2.6 Numerical analysis of a simple cubic/BCC architected solid

Details described in supporting materials.

3. Results

EMB3D printing entails extruding the printing ink into a supporting matrix, in which the embedded ink is immobilized, preserving its precise placement (Fig. 1A). The existence of the supporting matrix facilitates nozzle translation of nozzle in all positions, which enables ink deposition in a three-dimensional space. This distinctive feature allows the printing of highly complex geometries, for example, an Octet lattice, and a body centered cubic (BCC)/simple cubic (SC) lattice (Fig. 1C). More importantly, it offers freedom of extrusion path in a 3D context, including Z-axis direction, offering fiber alignment in all 3D directions. Fig. 1C-i shows a picture of the extrusion paths in x-y plane, z-axis direction, and diagonal direction. In EMB3D printing, extrusion rate (R), the rate of ink flowing out of the nozzle, and nozzle translation rate (r), the speed of the nozzle moving within the supporting matrix, together determine the fiber orientation. By controlling the printing parameters, we are able to manage the fiber orientation in highly localized regions, thus producing

diverse fiber micro-structures in a single object (Fig. 1B). This paves the way for the fabrication of metamaterials with programmable properties. For example, Fig. 1D demonstrates the successful manipulation of a BCC/SC lattice structure's anisotropic nature, generated by varied stiffness of the <110> and <001> orientations, achieving either isotropic characteristic or even more extreme anisotropy (further details in later sections).

3.1 Matrix elasticity for high-fidelity printing

To enable high resolution EMB3D printing of engineered composites, a crucial requirement is the structural integrity, ensuring that the embedded structures remain undistorted upon the nozzle translation. In addition to the appropriate viscosity, compatibility and Herschel-Bulkley behavior of the ink and matrix (*38*), optimized printing path has been reported for minimizing the disruptive nozzle travel motion, albeit it requires sophisticated algorithm calculations and is highly topology dependent (*39*), as some disruptive travel is inevitable in many prints. Here we found an additional criterion for high-fidelity embedded printing, that is a strong solid-like behavior with high elastic response of the supporting matrix, indicated by a low tanδ (equal to G''/ G', G'' is the loss modulus and G' is the storage modulus). To investigate this phenomenon, we have prepared different supporting matrices by mixing silicone oil (serves as matrix fluid) with two silica nanoparticles, TS720 and M5. While these matrices exhibit overlapping viscosity, yield stress, and storage modulus, they display a distinctive tanδ (Fig. 2A~2C). M5 matrix has a tanδ of 0.015 before yielding, one order of magnitude lower than that of all TS720 matrices (value of 0.2), suggesting a higher elastic response (Fig. 2C). We compared the printing quality in these matrices by printing test structures (Fig. 2D, cross structure, printing path in Fig. S1; and 2E, pyramid structure;). Both tests revealed that M5 matrix yields better printing quality. A series of TS720 matrices with varying particle loadings were prepared. Despite possessing a wide range of viscosities, moduli, and yield stresses, these TS720 matrices all share a high tanδ. It can be seen that noticeable distortion of the horizontal lines is observed in all TS720 matrices (Fig. 2D ii), and the two tips of the pyramid are spatially separated (Fig. 2E ii). On the contrary, the addition of 5 wt% M5 to silicone oil initiated minimal displacement on the horizontal line (Fig. 2D iii), and the two tips are completely connected (Fig. 2E iii). As M5 matrix shares overlapping viscosity, yield stress, and storage modulus with the TS720 matrix (Fig.2A, B), the importance of a much lower tanδ is highlighted. The distortion of the embedded ink can occur even without direct contact with the nozzle, as the surrounding matrix yields under the stress field induced by the translating nozzle. The stronger elastic response of the M5 matrix leads to a more rapid stress drop from the nozzle compared to the TS720 matrices, offering minimal yielding of the matrix for less ink displacement. As such, we establish the role of matrix elasticity as an additional criterion for high-feature fidelity of embedded printing, irrespective of printing path and Herschel-Bulkley behavior.

3.2 Controlling fiber 3D alignment while maintaining EMB3D printing integrity

The optimized EMB3D printing allows the three-dimensional ink extrusion for fiber 3D alignment. The alignment is achieved through the shear fields generated from the combined effects of ink extrusion rate (R) and nozzle translation rate (r). We can control fiber orientation by modulating the rate ratio (Rr) of R (set at 5 mm/s) and r, from highly random (Rr = 6) to highly aligned (Rr = 1). The control can be realized in a 3D space, as illustrated by the multiple extruded beams in various directions, including the through-plane direction (Fig. S2A). SEM images (Fig. 3A, D, and Fig. S2C, D) illustrate the fiber arrangement in beams printed with different Rr. The fiber

topologies exhibit identical alignment at the same Rr, regardless of the extrusion directions, demonstrating simultaneous fiber alignment in both through-plane and in-plane directions. We also used X-ray microcomputed tomography (μXCT) for quantitative analysis. The alignment is characterized by the angle θ between the CF and the beam axial direction (Fig. S2B), the values of which are indicated by different colors. We introduce "alignment efficiency," denoting the proportion of CFs with $\theta < 45°$. Clearly, the beams with Rr = 1 comprise predominantly blue/green fibers that are parallel to the axial direction, giving a 79.4% alignment efficiency and a peak distribution at 15º (Fig. 3B, C). As a comparison, a notable presence of red fibers (perpendicular to axial direction) is observed at Rr = 4 with only 39.0% alignment efficiency and a peak distribution at 50º (Fig. 3E, F). The fiber alignment of other Rr was also measured (Fig. 3G, Fig. S3) which follows the trend that higher Rr leads to higher peak angle and lower alignment efficiency. The worsened fiber alignment at higher Rr is due to the over-extrusion when ink exits the nozzle faster than the nozzle translation in the matrix. This disrupts the axial shear field for fiber alignment, as the ink tends to have outward flow directions.

On the other hand, the outward flow enlarges the beam diameter, as excess ink is pushed outward for lateral expansion (Fig. 3G). Beam diameter affects the EMB3D printing quality, as thicker beams generate stronger connection at the beam nodes. Fig. 3H shows the quantitatively analyzed result of the connection strength from a testing "cross" shape. The beams fail to be chemically bonded, indicated by the normalized force < 1, when Rr drops below 1.75 (more details discussed in supporting information). Consequently, lowering Rr yields better alignment, but compromises the printing fidelity. To address this, we implemented pausing time at the node for extra ink extrusion at lower Rr. The connection strength of each Rr with pausing time from 0s to 1s was examined (Fig. S4), and the data provides valuable guidance for selecting printing parameters when modulating Rr to control fiber alignment.

3.3 Three-dimensional property enhancement

The three-dimensional fiber alignment in our EMB3D-printed composites gives rise to property enhancement across all directions, especially for the through-plane directions, a longstanding challenge of the existing engineered composites (*40, 41*). Here we examined the stiffness and heat dissipation, as they are crucial for many composite applications. Both tests confirm the significant property enhancement in complete three-dimensional directions. The through-plane heat transfer was tested by placing printed lattices on top of a heating source (100 ºC) and the temperature change of the top of the lattices was monitored by using an infrared (IR) camera (Fig. 4A). We compared the performance of composites of pure epoxy, epoxy with random CF (epoxy-rCF, printed at Rr = 4), and aligned CF (epoxy-aCF, printed at Rr = 1), of which the fiber arrangement was confirmed by μXCT (Fig. 4B). The results (Fig. 4C, Fig. S5) illustrate that the vertically aligned CFs generate the highest maximum temperature and fastest heating rate, indicating the most substantial enhancement of heat transfer in Z-axis direction, which is noticeably better than random CF. This is attributed to the sequence of straight head-to-tail connections of aligned CF offering the shortest path for heat flux in the vertical direction compared to that offered by random fibers. Using the same sample compositions, we printed simple cubes and flexural bars at various orientations (0º, 45º and 90º) and measured their compressive and bending stiffness (Fig. 4D). It is evident that when the CF is properly aligned, the Young's modulus and flexural modulus increased 45.7% and 55.6% from random fiber, respectively, while the ultimate strain remains nearly unchanged (Fig. 4D, Fig. S6). This significant enhancement in stiffness is realized solely

from internal fiber arrangement control by modulating the Rr, without any changes to external architecture or material structure/composition. Furthermore, nearly identical stress-strain curves are observed from samples with the same fiber alignment but printed at different orientations (0º, 45º and 90º) in both compression and flexural tests. The isotropic mechanical performance signifies the achievement of simultaneous stiffness enhancement in both in-plane and through-plane directions induced by the 3D fiber alignment.

3.4 Metamaterial composite lattice with programmable elastic anisotropy

Engineered materials with tunable properties are highly sought after as they suit diverse requirements, such as directional reinforcing characteristics in aerospace and automotive industries (*42–44*). The above demonstrated ability to change the mechanical behavior by tuning the fiber arrangement enables our EMB3D printing to produce engineered composites with programmable anisotropic ratios and directional stiffness with the same 3D architecture. This can be achieved simply by modulating the rate ratio (Rr) at specific regions within the 3D lattice layout. Here we use the hybrid unit cell as an example. The cell is comprised of two sub-cells with distinct symmetries, namely simple cubic (SC) and body centered cubic (BCC) subunit cells, which together show an anisotropic stiffness tensor (Fig. 5A, B). By combining the experimental data and numerical calculations (Fig. 5C), we demonstrated that designing the fiber alignment within these two-symmetry groups allows us to program the stiffness anisotropy ratios of the unit cells, spanning from highly anisotropic to isotropic behavior. As shown in Fig. 5A, we have printed lattice cubes composed of four distinct SC/BCC designs and coded the fiber orientation as "a" (aligned CF) and "r" (random CF): 1) SC and BCC with aligned CF (abbreviated as SC-a/BCC-a), 2) SC and BCC with random CF (SC-r/BCC-r), 3) SC with aligned CF, BCC with random CF (SC-a/BCC-r), 4) SC with random CF, BCC with aligned CF (SC-r/BCC-a). Each design has been experimentally tested and numerically calculated at the <001> and <110> directions (Fig. 5B, details in supporting information, Fig. S7, 8). In the polar graph, we used azimuthal coordinate to represent the load direction, and the radial coordinate for the Young's modulus, which increases outward radially. The distinct anisotropies of the different designs can be visualized in "orientation spheres", with the cut plane through the sphere representing the polar plot (Fig. 5D). Numerical and experimental data show excellent agreement, confirming the accuracy of the numerical design and predictions. The stiffness anisotropy of the metamaterial was quantitatively examined by effective anisotropic ratio, A (*45*):

$$A = \frac{2(1+\nu)G}{E}$$

Where ν is the Poisson's ratio during the compression at <001> orientation, E is the Young's modulus of <001> orientation, and G is the shear modulus of <001> orientation (see supplemental information). The samples with original structure, including SC-a/BCC-a and SC-r/BCC-r exhibit an anisotropic ratio of 1.5 (Fig. S9, 10), consistent with the known anisotropic nature of the SC/BCC lattice (*46*). We converted this anisotropic nature to isotropic behavior by designing the SC-a/BCC-r structure, which shows an identical modulus at all orientations. On the other hand, the anisotropic ratio of the original structure is increased to 2.5 when SC-r/BCC-a design is applied. Again, the capability of changing the anisotropic ratio and directional moduli of a given lattice is solely achieved by varying meso-scale fiber arrangement, while the composites have identical lattice topology, material composition, and density.

4. Discussion

We have developed an EMB3D printing method for carbon fiber/epoxy composites, enabling simultaneous through-plane and in-plane fiber alignment. This approach has led to significant enhancements in mechanical properties and thermal conductivity in a three-dimensional context. It also generates engineered composites with programmable stiffness anisotropy and directional moduli. Our formulations of ink and supporting matrix incorporate optimized rheological properties to ensure high printing resolution for complex lattice architectures with meso-scale 3D alignment. Additionally, we have demonstrated the ability to adjust fiber alignment at specific regions by varying the rate ratio during printing, enabling precise control over localized micro-structures. By integrating regional fiber orientation with macro-architectural design, we have achieved the fabrication of 3D metamaterial lattices, effectively converting its anisotropic nature to isotropic behavior. An expanded degree of freedom of local fiber orientation control within the 3D matrices can be achieved by expanding the kinematics of nozzle movement to a 5-axis system. Furthermore, a multi-nozzle system can be incorporated to parallelize the extrusion process and print multiple struts at once in a single motion system. This study paves the way to control structural behaviors via synergistic control of meso-scale alignment and 3D macro-architectures, which opens new opportunities to manage conflicting material properties for multiple applications.

ACKNOWLEDGMENTS

Funding: This work was sponsored by the U.S. Department of Energy, Office of Energy Efficiency and Renewable Energy, Industrial Technologies Program, under contract DE-AC05-00OR22725 with UT-Battelle, LLC.

Author Contributions: V.S.D. and X.Z. designed research; Q.C., S.S.S., S.Z., A.J.D.S., Z.X., and J.Y.P., performed research; Q.C., S.S.S., S.Z., A.J.D.S., analyzed data; and Q.C., S.S.S., S.Z.; A.J.D.S., S.K., N.S.H., H.H. V.S.D. and X.Z. wrote the paper.

Copyright statement

This manuscript has been authored by UT-Battelle, LLC under Contract No. DE-AC05-00OR22725 with the U.S. Department of Energy. The United States Government retains and the publisher, by accepting the article for publication, acknowledges that the United States Government retains a non-exclusive, paid-up, irrevocable, world-wide license to publish or reproduce the published form of this manuscript, or allow others to do so, for United States Government purposes. The Department of Energy will provide public access to these results of federally sponsored research in accordance with the DOE Public Access Plan (http://energy.gov/downloads/doe-public-access-plan).

References

1. R. M. Erb, R. Libanori, N. Rothfuchs, A. R. Studart, Composites reinforced in three dimensions by using low magnetic fields. *Science* **335**, 199–204 (2012).
2. A. K. Pearce, T. R. Wilks, M. C. Arno, R. K. O'Reilly, Synthesis and applications of anisotropic nanoparticles with precisely defined dimensions. *Nature Reviews Chemistry* **5**, 21–45 (2021).
3. I. M. Daniel, O. Ishai, I. M. Daniel, I. Daniel, *Engineering mechanics of composite materials* (Oxford university press New York, 1994).
4. R.-F. Guo, Z.-J. Hu, A. Shaga, P. Shen, Development of a nacre-like metal-ceramic composite with a brick-and-mortar structure and high ceramic content. *Composites Part A: Applied science and manufacturing* **165**, 107347 (2023).
5. T. Slawik, A. Bergner, R. Puschmann, P. Franke, J. Raethel, T. Behnisch, R. Scholl, L.-M. Berger, T. Moritz, R. Zelm, others, Metal‐ceramic layered materials and composites manufactured using powder techniques. *Advanced Engineering Materials* **16**, 1293–1302 (2014).
6. M. E. Launey, M. J. Buehler, R. O. Ritchie, On the mechanistic origins of toughness in bone. *Annual review of materials research* **40**, 25–53 (2010).
7. E. Marklund, J. Varna, Modeling the effect of helical fiber structure on wood fiber composite elastic properties. *Applied Composite Materials* **16**, 245–262 (2009).
8. M. Li, Z. Ali, X. Wei, L. Li, G. Song, X. Hou, H. Do, J. C. Greer, Z. Pan, C.-T. Lin, others, Stress induced carbon fiber orientation for enhanced thermal conductivity of epoxy composites. *Composites Part B: Engineering* **208**, 108599 (2021).
9. S. Ghaffari-Mosanenzadeh, O. Aghababaei Tafreshi, E. Dammen-Brower, E. Rad, M. Meysami, H. E. Naguib, A review on high thermally conductive polymeric composites. *Polymer Composites* **43**, 692–711 (2022).
10. C. Zweben, in *Semiconductor Thermal Measurement and Management IEEE Twenty First Annual IEEE Symposium, 2005* (2005), pp. 168–174.
11. X. Pei, B. Shang, L. Chen, J. Li, Y. Tang, Compression properties of multilayer-connected biaxial weft knitted carbon fiber fabric reinforced composites. *Composites Part B: Engineering* **91**, 296–305 (2016).
12. J.-u. Jang, H. C. Park, H. S. Lee, M.-S. Khil, S. Y. Kim, Electrically and thermally conductive carbon fibre fabric reinforced polymer composites based on nanocarbons and an in-situ polymerizable cyclic oligoester. *Scientific reports* **8**, 7659 (2018).
13. U. Khan, P. May, A. O'Neill, A. P. Bell, E. Boussac, A. Martin, J. Semple, J. N. Coleman, Polymer reinforcement using liquid-exfoliated boron nitride nanosheets. *Nanoscale* **5**, 581–587 (2013).

14. M. G. Rasul, A. Kiziltas, B. Arfaei, R. Shahbazian-Yassar, 2D boron nitride nanosheets for polymer composite materials. *npj 2D Materials and Applications* **5**, 56 (2021).

15. X. Wang, M. Jiang, Z. Zhou, J. Gou, D. Hui, 3D printing of polymer matrix composites: A review and prospective. *Composites Part B: Engineering* **110**, 442–458 (2017).

16. Q. Chen, L. Han, J. Ren, L. Rong, P. Cao, R. C. Advincula, 4D printing via an unconventional fused deposition modeling route to high-performance thermosets. *ACS applied materials & interfaces* **12**, 50052–50060 (2020).

17. Q. Chen, P.-F. Cao, R. C. Advincula, Mechanically robust, ultraelastic hierarchical foam with tunable properties via 3D printing. *Advanced Functional Materials* **28**, 1800631 (2018).

18. R. L. Truby, M. Wehner, A. K. Grosskopf, D. M. Vogt, S. G. M. Uzel, R. J. Wood, J. A. Lewis, Soft somatosensitive actuators via embedded 3D printing. *Advanced materials* **30**, 1706383 (2018).

19. D. E. Yunus, W. Shi, S. Sohrabi, Y. Liu, Shear induced alignment of short nanofibers in 3D printed polymer composites. *Nanotechnology* **27**, 495302 (2016).

20. G. Ma, Z. Li, L. Wang, F. Wang, J. Sanjayan, Mechanical anisotropy of aligned fiber reinforced composite for extrusion-based 3D printing. *Construction and Building Materials* **202**, 770–783 (2019).

21. W. J. Wright, E. Celik, In situ electrical network activation and deactivation in short carbon fiber composites via 3D printing. *Advanced Functional Materials* **33**, 2303282 (2023).

22. N. S. Hmeidat, J. W. Kemp, B. G. Compton, High-strength epoxy nanocomposites for 3D printing. *Composites Science and Technology* **160**, 9–20 (2018).

23. B. G. Compton, J. A. Lewis, 3D-printing of lightweight cellular composites. *Advanced materials* **26**, 5930–5935 (2014).

24. Z. Liang, Y. Pei, C. Chen, B. Jiang, Y. Yao, H. Xie, M. Jiao, G. Chen, T. Li, B. Yang, others, General, vertical, three-dimensional printing of two-dimensional materials with multiscale alignment. *ACS nano* **13**, 12653–12661 (2019).

25. Y. Qian, C. Li, Y. Qi, J. Zhong, 3D printing of graphene oxide composites with well controlled alignment. *Carbon* **171**, 777–784 (2021).

26. M. K. Hausmann, P. A. Ruhs, G. Siqueira, J. Läuger, R. Libanori, T. Zimmermann, A. R. Studart, Dynamics of cellulose nanocrystal alignment during 3D printing. *ACS nano* **12**, 6926–6937 (2018).

27. B. G. Compton, N. S. Hmeidat, R. C. Pack, M. F. Heres, J. R. Sangoro, Electrical and mechanical properties of 3D-printed graphene-reinforced epoxy. *Jom* **70**, 292–297 (2018).

28. N. S. Hmeidat, D. S. Elkins, H. R. Peter, V. Kumar, B. G. Compton, Processing and mechanical characterization of short carbon fiber-reinforced epoxy composites for material extrusion additive manufacturing. *Composites Part B: Engineering* **223**, 109122 (2021).

29. N. S. Hmeidat, R. C. Pack, S. J. Talley, R. B. Moore, B. G. Compton, Mechanical anisotropy in polymer composites produced by material extrusion additive manufacturing. *Additive Manufacturing* **34**, 101385 (2020).

30. E. B. Trigg, N. S. Hmeidat, L. M. Smieska, A. R. Woll, B. G. Compton, H. Koerner, Revealing filler morphology in 3D-printed thermoset nanocomposites by scanning microbeam X-ray scattering. *Additive Manufacturing* **37**, 101729 (2021).

31. S. Safaee, M. Schock, E. B. Joyee, Y. Pan, R. K. Chen, Field-assisted additive manufacturing of polymeric composites. *Additive Manufacturing* **51**, 102642 (2022).

32. D. Kokkinis, M. Schaffner, A. R. Studart, Multimaterial magnetically assisted 3D printing of composite materials. *Nature communications* **6**, 8643 (2015).

33. R. R. Collino, T. R. Ray, R. C. Fleming, C. H. Sasaki, H. Haj-Hariri, M. R. Begley, Acoustic field controlled patterning and assembly of anisotropic particles. *Extreme Mechanics Letters* **5**, 37–46 (2015).

34. Z. Zhang, M. Li, Y. Wang, W. Dai, L. Li, Y. Chen, X. Kong, K. Xu, R. Yang, P. Gong, others, Ultrahigh thermal conductive polymer composites by the 3D printing induced vertical alignment of carbon fiber. *Journal of Materials Chemistry A* **11**, 10971–10983 (2023).

35. G. Fang, T. Zhang, Y. Huang, Z. Zhang, K. Masania, C. C. L. Wang, Exceptional mechanical performance by spatial printing with continuous fiber: Curved slicing, toolpath generation and physical verification. *Additive Manufacturing* **82**, 104048 (2024).

36. T. Zhang, T. Liu, N. Dutta, Y. Chen, R. Su, Z. Zhang, W. Wang, C. C. L. Wang, Toolpath generation for high density spatial fiber printing guided by principal stresses. *Composites Part B: Engineering*, 112154 (2025).

37. J. R. Raney, B. G. Compton, J. Mueller, T. J. Ober, K. Shea, J. A. Lewis, Rotational 3D printing of damage-tolerant composites with programmable mechanics. *Proceedings of the National Academy of Sciences* **115**, 1198–1203 (2018).

38. A. K. Grosskopf, R. L. Truby, H. Kim, A. Perazzo, J. A. Lewis, H. A. Stone, Viscoplastic matrix materials for embedded 3D printing. *ACS applied materials & interfaces* **10**, 23353–23361 (2018).

39. R. D. Weeks, R. L. Truby, S. G. M. Uzel, J. A. Lewis, Embedded 3D Printing of Multimaterial Polymer Lattices via Graph-Based Print Path Planning. *Advanced materials* **35**, 2206958 (2023).

40. Z.-G. Wang, W. Liu, Y.-H. Liu, Y. Ren, Y.-P. Li, L. Zhou, J.-Z. Xu, J. Lei, Z.-M. Li, Highly thermal conductive, anisotropically heat-transferred, mechanically flexible composite film by assembly of boron nitride nanosheets for thermal management. *Composites Part B: Engineering* **180**, 107569 (2020).

41. A. Osman, A. Elhakeem, S. Kaytbay, A. Ahmed, A comprehensive review on the thermal, electrical, and mechanical properties of graphene-based multi-functional epoxy composites. *Advanced Composites and Hybrid Materials* **5**, 547–605 (2022).

42. D. Ozkan, M. S. Gok, A. C. Karaoglanli, Carbon fiber reinforced polymer (CFRP) composite materials, their characteristic properties, industrial application areas and their machinability. *Engineering Design Applications III: Structures, Materials and Processes*, 235–253 (2020).

43. S. P. Haanappel, R. H. W. ten Thije, U. Sachs, B. Rietman, R. Akkerman, Formability analyses of uni-directional and textile reinforced thermoplastics. *Composites Part A: Applied science and manufacturing* **56**, 80–92 (2014).

44. S. H. Lee, S. Yu, F. Shahzad, W. N. Kim, C. Park, S. M. Hong, C. M. Koo, Density-tunable lightweight polymer composites with dual-functional ability of efficient EMI shielding and heat dissipation. *Nanoscale* **9**, 13432–13440 (2017).

45. Z. Chen, Y. M. Xie, X. Wu, Z. Wang, Q. Li, S. Zhou, On hybrid cellular materials based on triply periodic minimal surfaces with extreme mechanical properties. *Materials & design* **183**, 108109 (2019).

46. T. Tancogne-Dejean, D. Mohr, Elastically-isotropic truss lattice materials of reduced plastic anisotropy. *International Journal of Solids and Structures* **138**, 24–39 (2018).

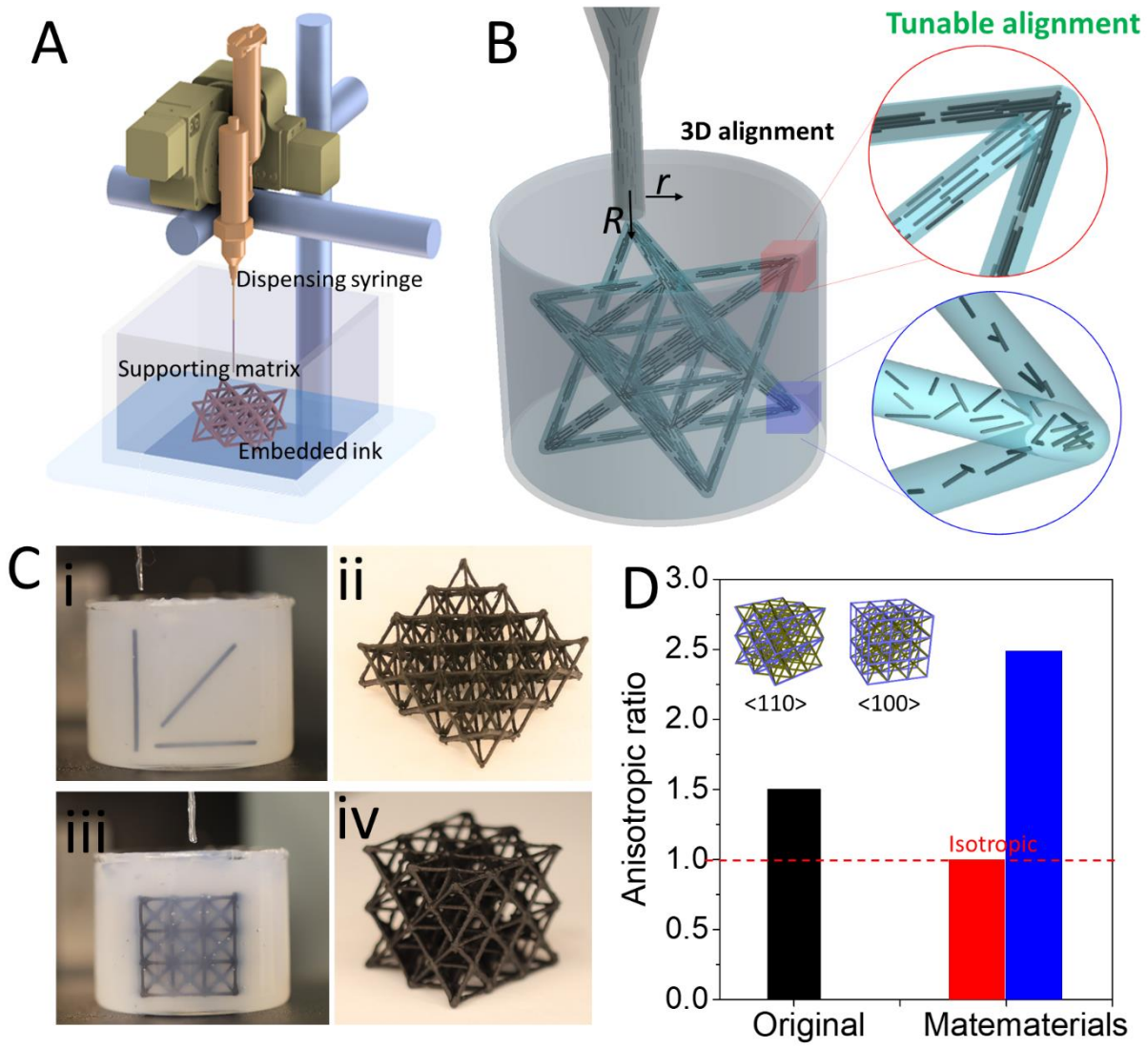

Fig. 1. Embedded 3D printing with 3D fiber alignment. A) Schematic of EMB3D printing process. B) Illustration of controlled carbon fiber 3D alignment at specific regions. C) Images of different EMB3D printed structures. i) extrusion of ink in x-y plane, along z-axis, and diagonal direction. ii) Octet lattice; iii) completed printing of BCC/SC lattice; iv) <110> orientation of BCC/SC lattice. D) Manipulation of anisotropic ratio of lattice structure by varying fiber alignment in a 3D context. Insert: <110> and <001> orientation of the BCC/SC lattice.

1

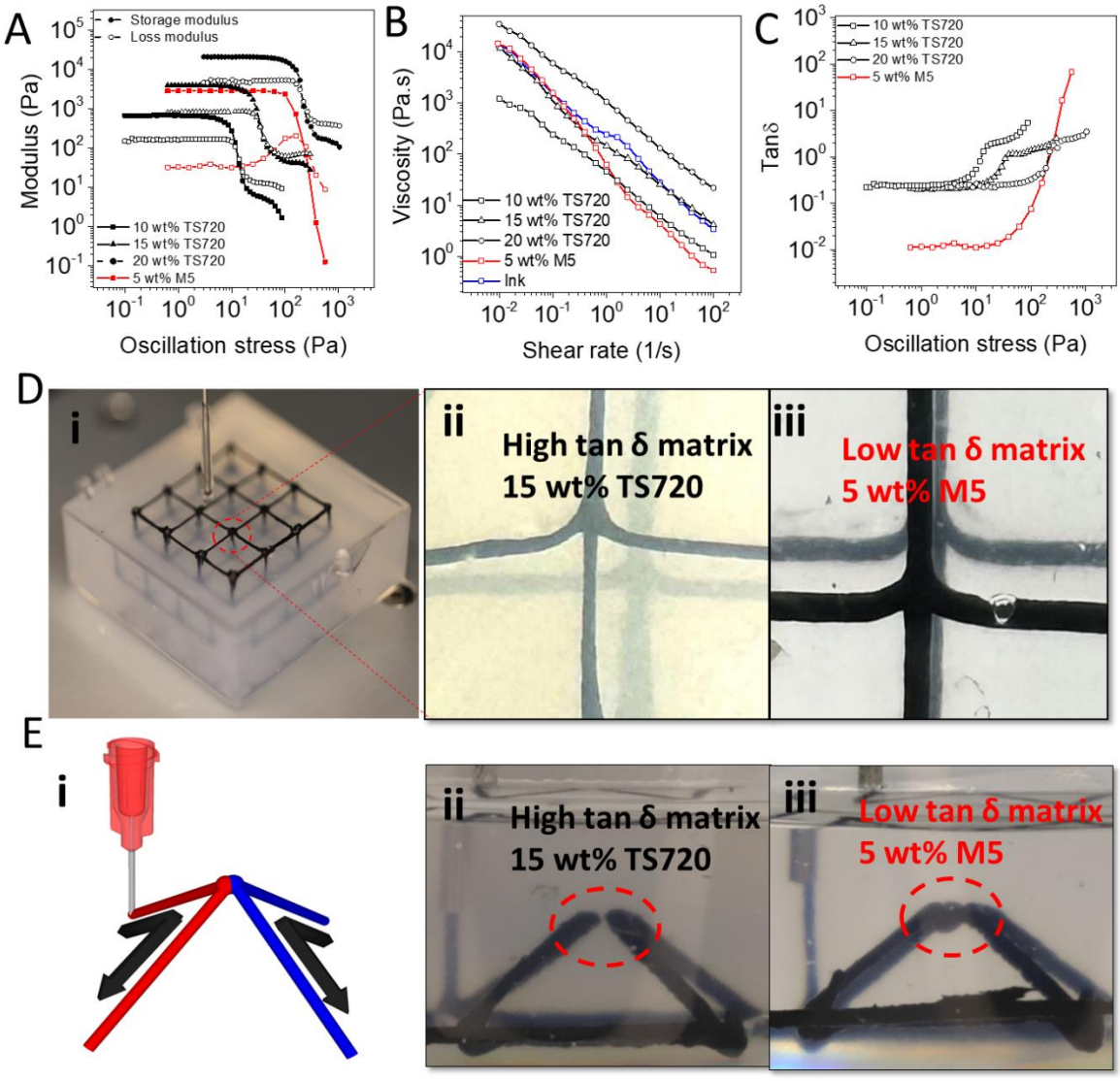

Fig. 2. **Optimized matrix rheology with high elastic response for high-fidelity EMB3D printing.** A) Log-log plot of the storage modulus, G', and loss modulus, G", as a function of shear stress for matrices prepared with different fumed silica nanoparticles. B) Viscosity as a function of shear stress of different matrix compositions C)Tanδ as a function of shear stress of different matrix compositions. D) Optical images of the printed "cross" structures for printing quality illustration. (i) completed printing of "cross" structure, (ii) structure printed in matrix with high tanδ (TS720 matrices) and (iii) structure printed in matrix with low tanδ (M5 matrix). E) Optical images of the printed pyramid structure for the printing quality illustration. (i) colored printing path, (ii) structure printed in TS720 matrices and (iii) structure printed in

1

1

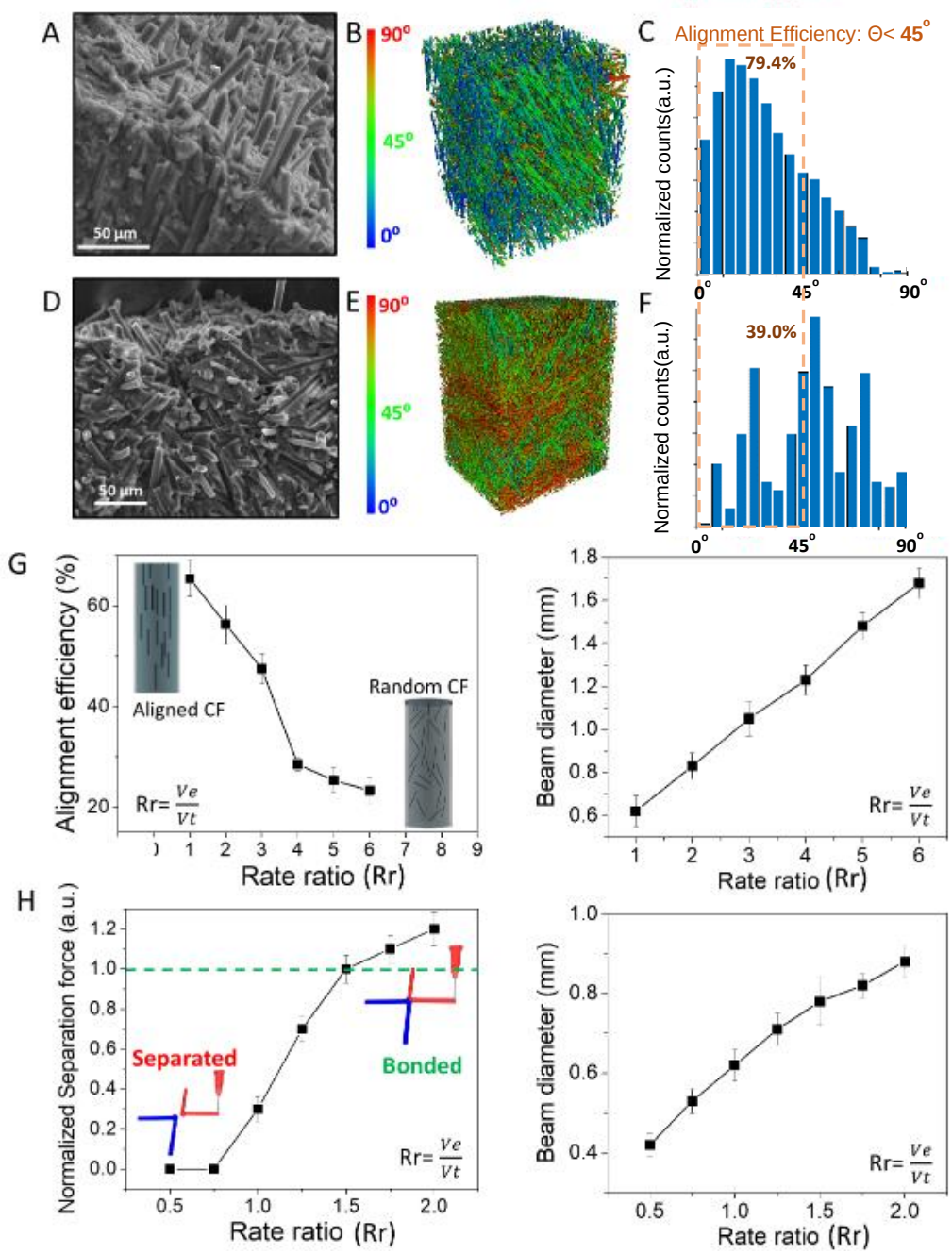

Fig. 3. Controlling fiber 3D alignment and maintaining printing quality by tuning rate ratio of extrusion rate and nozzle translation rate. A)-C): Samples extruded by rate ratio =1 at θ = 90º, D)-F): Samples extruded by rate ratio = 4 at θ = 90º. A, D) SEM images of cross-sections of extruded beams. B, E) Reconstructed models with angle distribution of μXCT scan results. C, F) angle distribution plots of aligned CFs. G) Beam size and alignment efficiency at different rate ratios. Insert: fiber alignment illustration. H) Beam size and the separation force at different rate ratios. Insert: printing bath of the "cross"

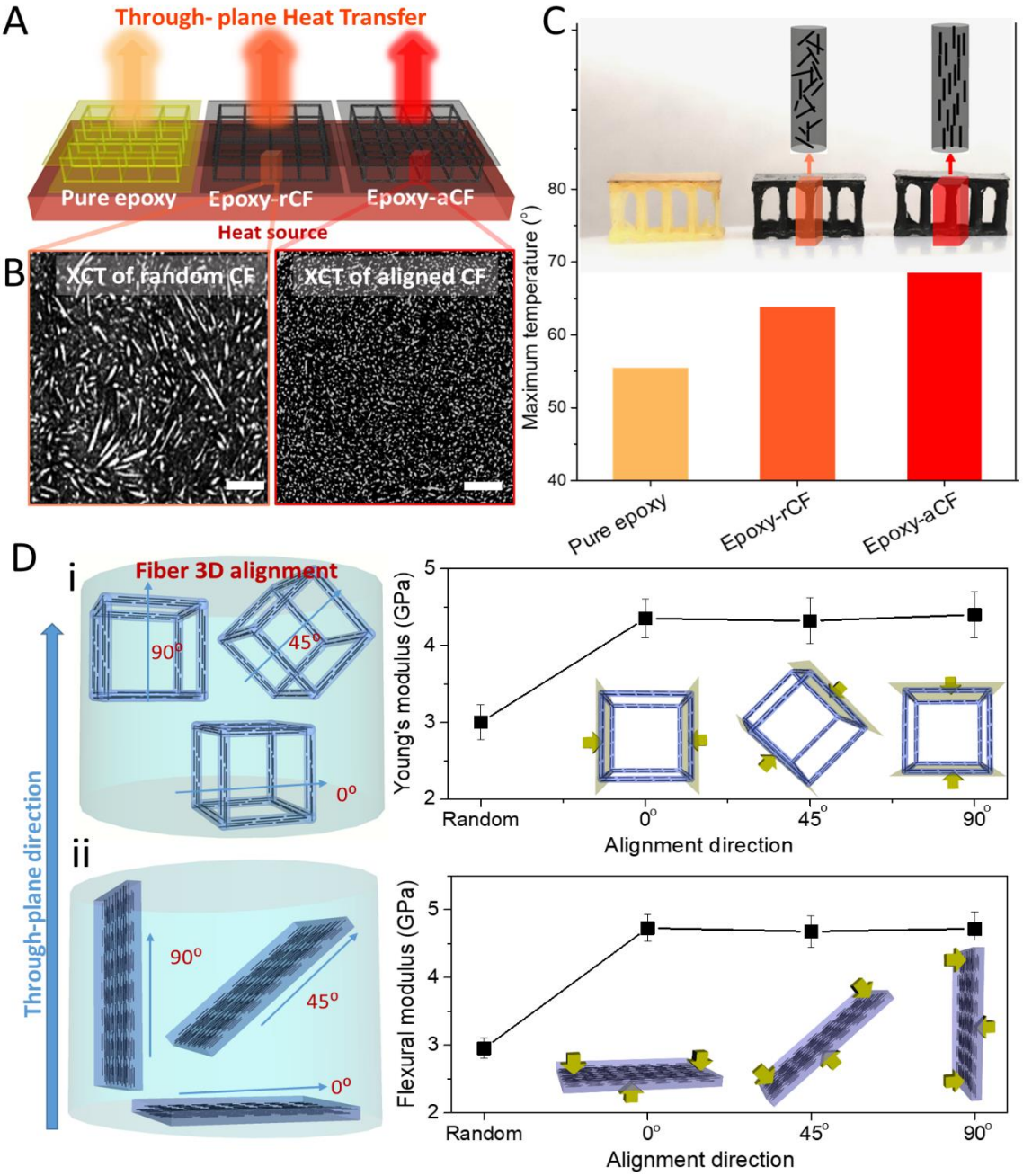

Fig. 4. Three-dimensional properties enhancement by 3D fiber alignment. A) Illustration of heat transfer measurement. B) μXCT images of top-view cross-section of vertical beams with random and aligned carbon fibers. C) Optical images of samples of pure epoxy, epoxy-rCF, epoxy-aCF, and their corresponding maximum temperatures after heat transfer. D) Mechanical tests of samples printed at various directions in a 3D space. i) Compression test of simple cubes with varying fiber alignment directions. ii) Flexural test of flexural specimens with varying fiber alignment directions.

1

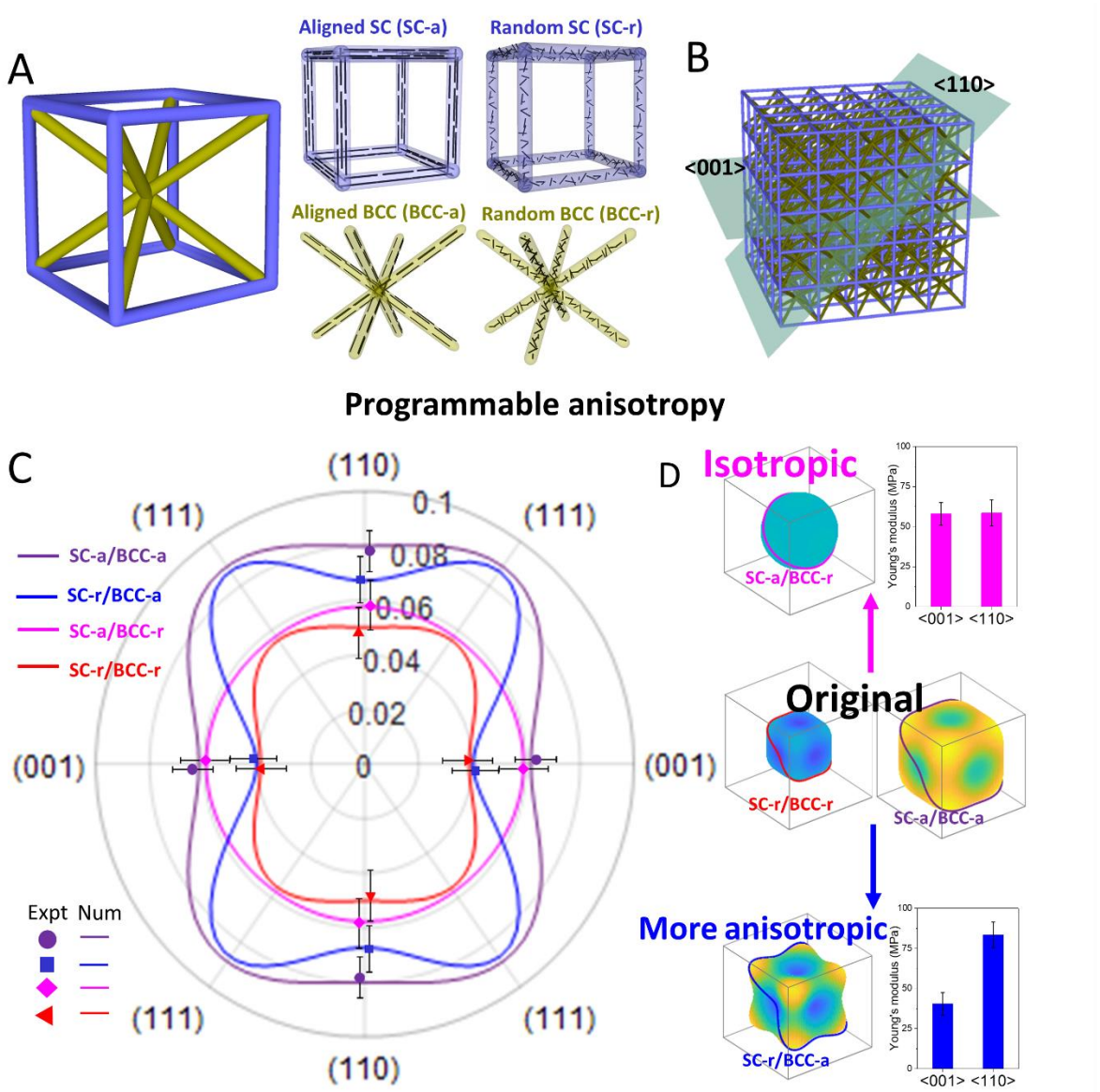

1

Fig. 5. Programmable anisotropy *via* tuning regional fiber 3D alignment. A) Schematic of the unit lattice cell composed of simple cubic (SC) and body centered cubic (BCC) subcells, each subcell with distinct random and aligned fiber designs. B) Schematics of the <001> and <110> orientations. C) Polar graph of numeric predictions and experimental data: Young's modulus as function of the orientation of the compression with respect to the unit cell lattice vectors. D) Modulating the stiffness anisotropic ratio by varying the fiber 3D alignment. Within the cube frame representing the edges of unit cell, shaped solids indicate the directional value of Young's modulus in radial distance from the cube center and in color. Color indicates value from most compliant (blue) to stiffest (yellow). All cubes share the same color axis.